LETTER

doi:10.1038/nature11231

Terahertz-field-induced insulator-to-metal transition in vanadium dioxide metamaterial

Mengkun Liu[1]*, Harold Y. Hwang[2]*, Hu Tao[3], Andrew C. Strikwerda[1], Kebin Fan[4], George R. Keiser[1], Aaron J. Sternbach[1], Kevin G. West[5], Salinporn Kittiwatanakul[5], Jiwei Lu[5], Stuart A. Wolf[5,6], Fiorenzo G. Omenetto[3], Xin Zhang[4], Keith A. Nelson[2] & Richard D. Averitt[1]

Electron–electron interactions can render an otherwise conducting material insulating[1], with the insulator–metal phase transition in correlated-electron materials being the canonical macroscopic manifestation of the competition between charge-carrier itinerancy and localization. The transition can arise from underlying microscopic interactions among the charge, lattice, orbital and spin degrees of freedom, the complexity of which leads to multiple phase-transition pathways. For example, in many transition metal oxides, the insulator–metal transition has been achieved with external stimuli, including temperature, light, electric field, mechanical strain or magnetic field[2–7]. Vanadium dioxide is particularly intriguing because both the lattice and on-site Coulomb repulsion contribute to the insulator-to-metal transition at 340 K (ref. 8). Thus, although the precise microscopic origin of the phase transition remains elusive, vanadium dioxide serves as a testbed for correlated-electron phase-transition dynamics. Here we report the observation of an insulator–metal transition in vanadium dioxide induced by a terahertz electric field. This is achieved using metamaterial-enhanced picosecond, high-field terahertz pulses to reduce the Coulomb-induced potential barrier for carrier transport[9]. A nonlinear metamaterial response is observed through the phase transition, demonstrating that high-field terahertz pulses provide alternative pathways to induce collective electronic and structural rearrangements. The metamaterial resonators play a dual role, providing sub-wavelength field enhancement that locally drives the nonlinear response, and global sensitivity to the local changes, thereby enabling macroscopic observation of the dynamics[10,11]. This methodology provides a powerful platform to investigate low-energy dynamics in condensed matter and, further, demonstrates that integration of metamaterials with complex matter is a viable pathway to realize functional nonlinear electromagnetic composites.

Ultrafast spectroscopic techniques are important for investigating phase-transition dynamics, because they can be used to initiate changes, and provide sufficient time resolution to monitor excited states or metastable order parameters not accessible with time-integrated measurements[6,7,12,13]. Indeed, recent ultrafast pump–probe measurements on vanadium dioxide (VO_2) with near-infrared pulses revealed that excitation of electrons across the insulating Hubbard gap results in percolative metallicity on a picosecond timescale[12,13]. Direct-current electric fields of $\sim$100 kV cm^{-1}also induce the insulator-to-metal transition (IMT), but do not permit measurement of the field-induced transition dynamics[9,14]. From existing direct current (d.c.) measurements it has not been clear whether ultrafast electric fields could induce the IMT, or what the timescale would be.

Recent developments have enabled the generation of ultrafast terahertz (THz) pulses with field levels of 0.1–1 MV cm^{-1} (refs 15–17). Time-resolved THz pump–probe measurements have revealed dynamic electronic responses initiated by such high fields[15,18]. THz probe pulses are ideally suited to monitor the IMT, as they provide a direct measure of the conductivity in the GHz–THz frequency range. Figure 1a shows the temperature-dependent far-infrared conductivity (σ_1) of our 75-nm VO_2 film deposited on a sapphire substrate[19]. The results were obtained by fitting a Drude response to the transmission from a conventional THz time-domain spectroscopy (THz-TDS) measurement using low-field THz pulses[6,13]. The IMT occurs at 340 K, and in the high-temperature rutile phase the conductivity of $\sim$5,000 $(\Omega\,\mathrm{cm})^{-1}$ is comparable to that of bulk single-crystal VO_2. Hysteresis, associated with the first-order structural transition, is also observed. Below 330 K, the conductivity is below our detection limit with conventional THz-TDS. For intense THz excitation, we deposited metamaterial structures that served as local resonant THz concentrators. Using gold split-ring resonators (SRRs), which are essentially sub-wavelength *LC* circuits, the THz electric field inside the SRR capacitive gap can be enhanced by more than an order of magnitude.

Figure 1b shows an optical image of the 200-nm-thick gold SRRs that we deposited onto a VO_2 film. The SRR lateral dimension is 76 μm, with a periodicity of 100 μm. For our experiments, the most important regions are the 1.5-μm SRR capacitive gaps that are oriented horizontally, where the vertically polarized THz field is enhanced. For these SRRs, the *LC* resonance, shown in Fig. 1c (300-K data) is at 0.41 THz, whereas the pure electric-dipole resonance (which would occur in the gap with just the two adjacent vertical gold segments forming a dipole antenna) is at $\sim$1 THz (ref. 20). In addition to THz field enhancement in the gaps, the SRR structures provide exquisite sensitivity for THz probing of small changes in the VO_2 thin-film transmission near the phase transition, where the conductivity is small. Although only a small fraction of the THz probe radiation directly irradiates the gaps, the resonant behaviour of the entire SRR array is affected profoundly by the in-gap VO_2 properties. Figure 1c shows the frequency-dependent SRR/VO_2 response as a function of temperature, measured using low-field THz-TDS. The SRR gap is gradually shorted as the VO_2 becomes metallic, leading to a transmission increase at the resonance frequency with increasing temperature. The inductive-capacitive resonance *LC* disappears at $\sim$350 K, corresponding to a film conductivity of $\sim$200 $(\Omega\,\mathrm{cm})^{-1}$. From 300 to 340 K, there is a small but perceptible redshift of the *LC* resonance due to increasing permittivity of the VO_2 film associated with percolation of the metallic phase. A small hysteresis in the transmission is also observed (not shown), analogous to that shown in Fig. 1a and observed in previous experiments[21]. The higher-frequency dipolar resonance also shows a redshift, because the effective dipole length increases as the SRR gaps are shorted. As Fig. 1c shows, the SRRs provide enhanced conductivity sensitivity to changes in the material properties within the gaps. Thus,

[1]Department of Physics, Boston University, Boston, Massachusetts 02215, USA. [2]Department of Chemistry, Massachusetts Institute of Technology, Cambridge, Massachusetts 02139 USA. [3]Biomedical Engineering, Tufts University, Medford, Massachusetts 02155, USA. [4]Department of Mechanical Engineering, Boston University, Boston, Massachusetts 02215, USA. [5]Department of Materials Science and Engineering, University of Virginia, Charlottesville, Virginia 22904, USA. [6]Department of Physics, University of Virginia, Charlottesville, Virginia 22904, USA.
* These authors contributed equally to this work.

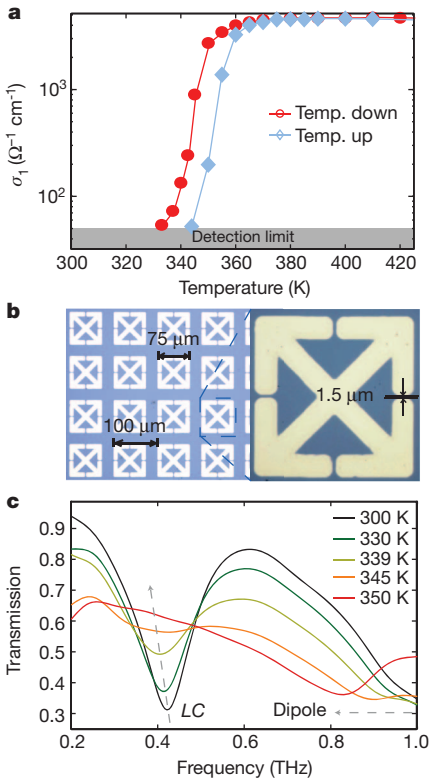

Figure 1 | Low-field THz characterization of 75-nm VO_2 thin film on sapphire with and without metamaterials. **a**, Temperature-dependent far-infrared conductivity (σ_1) of bare VO_2 thin film (75 nm thick) on sapphire substrate measured by THz-TDS. σ_1 was obtained by fitting the THz transmission to a standard Drude response. **b**, Optical image of metamaterial split-ring resonators (SRRs) deposited on VO_2/sapphire. The SRR gap is 1.5 μm. **c**, Temperature-dependent THz transmission spectra of SRRs on VO_2. *LC* and dipole resonances as described in text.

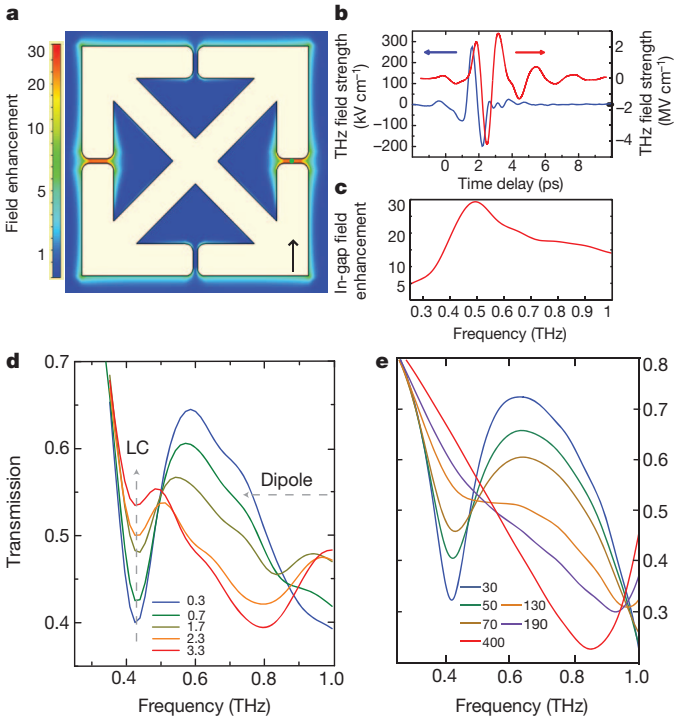

Figure 2 | Full-wave simulations of the electric field enhancement in the SRR and nonlinear THz transmission experiment. **a**, Resonant field enhancement as a function of position. **b**, Simulated time-dependent THz field (red) in the horizontal gaps using experimental data (blue) as the input. **c**, Frequency-dependent in-gap field enhancement obtained from the ratio of Fourier amplitudes of the simulated in-gap and measured incident fields in **b**. **d**, Experimental data showing field-dependent nonlinear transmission spectra of SRRs on VO_2 at 324 K, for in-gap fields ranging from 0.3 to 3.3 MV cm^{-1}. **e**, Full-wave simulations of SRR response for in-gap conductivities ranging from 30 to 400 $(\Omega\,\mathrm{cm})^{-1}$ (assuming σ_1 changes only in the gaps).

in the following nonlinear dynamics measurements, SRRs provide local excitation by field enhancement in the capacitive gaps and global sensitivity to the induced changes in the VO_2 within the gaps.

Full-wave electromagnetic simulations reveal the spatiotemporal features of the field enhancement in the SRRs (see Supplementary Information). Figure 2a shows that in the horizontally oriented gaps, there is a 27-fold field enhancement at the *LC* resonance frequency. Figure 2b shows the simulated time-dependent electric field (red curve) in the middle of the horizontal gaps, with the experimentally measured THz field (blue curve) used as input for the simulation. An incident peak field amplitude of ~300 kV cm^{-1} leads to a peak field of 4 MV cm^{-1} in the gap. Fourier transformation of the time-domain field profiles in Fig. 2b and calculation of the ratio of the spectral amplitudes yields the field enhancement as a function of frequency, as shown in Fig. 2c. The field enhancement is quite broadband as a result of the breadth and close proximity of the *LC* and electric-dipole modes. The magnitude of the calculated field enhancement is consistent with calculated and experimental results recently obtained on simpler antenna structures[20,22,23].

Figure 2d shows the experimentally measured nonlinear response of SRRs on VO_2 that is initially in the insulating state (324 K). These single-beam measurements show that the transmission at the *LC* resonance frequency (0.41 THz) increases with increasing incident field. Given the temperature-dependent data in Fig. 1c, this is consistent with an increase in the VO_2 conductivity in the SRR gaps. The higher-frequency dipole also redshifts as the in-gap VO_2 conductivity increases (peak at ~0.8 THz for the highest incident fields). At the highest field strength below damage threshold, the average conductivity increase is above 500 $(\Omega\,\mathrm{cm})^{-1}$, as estimated by the dipole frequency shift. Simulations assuming that the conductivity change occurs only within the horizontal gaps (Fig. 2e) agree well with experiment, although the measured resonance does not completely vanish. This is probably because the Gaussian-like THz beam profile leads to a larger effect in the centre of the beam than at the edge, where the THz field is weaker, and averaging of the measurement over the beam profile is not accounted for in the simulations.

The results in Fig. 2 clearly indicate a nonlinear response, but additional measurements are required to determine the dynamic response, which could suggest its probable microscopic origins. Figure 3 shows the time-dependent transmission of a weak-field THz probe pulse that was variably delayed with respect to the high-field THz pump pulse at an in-gap field strength of ~1 MV cm^{-1} (below the damage threshold). A plot of transmission as a function of frequency and pump–probe delay (Fig. 3a) shows the temporal evolution of the THz spectral response. From these data it is clear that the 0.41-THz *LC* resonance transmission increases, whereas the 1.0-THz dipole resonance exhibits a frequency shift. These changes occur on a picosecond timescale, as the VO_2 conductivity increases towards that of the metallic phase. Linescans (Fig. 3b,c)more clearly reveal the dynamics. The time constants for initial change in transmission at 0.41 and 0.8 THz are 7 and 9 ps respectively, comparable to what has been observed in optical-pump, THz-probe experiments and consistent with a percolative phase transition[6,7,13]. The intrinsic conductivity response may be even faster, as the THz pump fields in the gaps are time-broadened (Fig. 2b). Nonetheless, it is clear that the THz pump induces a rapid change in the in-gap VO_2 conductivity. The change persists with little or no relaxation during the 100-ps range of our pump–probe time delay.

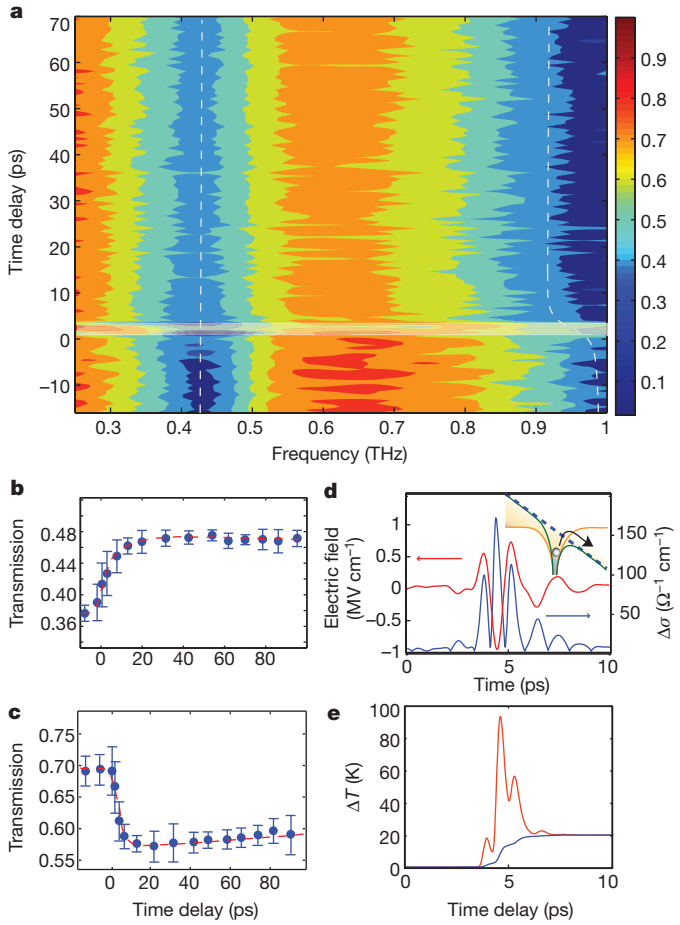

Figure 3 | THz pump–probe measurement and model calculation. **a**, Two-dimensional experimental data at 1 MV cm^{-1} in-gap field strength. The colour scale shows the transmission (unitless). **b** and **c**, Line-scans at (**b**) 0.41 THz, the metamaterial *LC* resonance, and (**c**) 0.8 THz, the metamaterial dipole resonance. Blue dots, data (324 K, 1 MV cm^{-1}); red curves, exponential fits. Error bars show standard error of the mean ($n = 8$). **d**, The in-gap electric field (red curve) results in a reduction of the confining potential (see inset), leading to the calculated Poole–Frenkel conductivity (blue curve). This releases carriers, leading to an absorbed power density that heats the electrons and subsequently the lattice, driving the VO_2 IMT. **e**, Electron (red) and lattice (blue) temperatures calculated using equation (2) (see text).

Our analysis suggests a two-step process (see Supplementary Information) for the THz-induced phase transition. First, the electric field reduces the Coulomb-induced activation barrier for carrier motion. This can be modelled by the Poole–Frenkel (PF) effect, described as[24,25]

$$\sigma = \sigma_0 \exp\left(\frac{\beta\sqrt{|E(t)|}}{rk_BT}\right) \quad (1)$$

where σ is the conductivity, σ_0 is the initial conductivity, $E(t)$ is the electric field, T is the temperature, and $\beta = (e^3/\pi\varepsilon)^{1/2}$ is the PF constant, where ε is the dielectric constant and r is a constant that depends on the position of the Fermi level. The PF effect contributes to the early dynamics of the IMT while the THz field is still acting on the sample. The electric field lowers the potential barrier to carrier hopping, increasing the carrier density[24–26]. A calculation of the transient PF conductivity is shown in Fig. 3d, along with a schematic illustration of the field-induced barrier reduction. The peak conductivity change ($\sim$150 (Ω cm)$^{-1}$) is consistent with the conductivity required to obtain the experimental transmission changes shown in Figs 2 and 3. In principle, if the carrier number density reaches the critical value ($\sim 10^{21}$ cm^{-3}) obtained by a modified Mott criterion for VO_2 (ref. 26), the PF effect alone would be sufficient to induce the IMT. However, as we now discuss, thermal effects rapidly follow the PF dynamics.

The PF-induced increase in carrier density serves as the initial condition for subsequent electric-field-induced carrier acceleration, leading to Joule heating through electron-lattice coupling[27]. This results in a temperature increase that drives the VO_2 into the persistent metallic phase. This can be modelled approximately with the well-known two-temperature model, describing the temporal evolution of the energy density in the electrons and lattice:

$$C_e\frac{dT_e}{dt} = -G(T_e - T_i) + \sigma(t)E^2(t)$$
$$C_i\frac{dT_i}{dt} = +G(T_e - T_i) \quad (2)$$

T_e (C_e) and T_i (C_i) are the temperature (specific heat) of the electrons and lattice, respectively, and G is the electron–phonon coupling coefficient, all of which have been determined experimentally for VO_2. The energy density from the incident electric field is approximated as $\sigma(t)E^2(t)$. Using the PF conductivity calculated in Fig. 3d and the experimental electric field (peak in-gap field 1 MV cm^{-1}), the above equation can be solved for T_e and T_i as a function of time, as shown in Fig. 3e. The initial electron heating dynamics, which approximately follow the THz intensity profile, are followed by equilibration of the lattice and electronic temperatures. The calculations indicate an increase of the VO_2 lattice temperature by $\sim$20 K on a several-picosecond timescale, consistent with the measured dynamics. The dynamics are clearly more complex than in our simple model, as the field enhancement decreases as the conductivity increases within the gaps. Nonetheless, THz-induced carrier release and acceleration followed by Joule heating on a picosecond timescale seems very likely to be the IMT

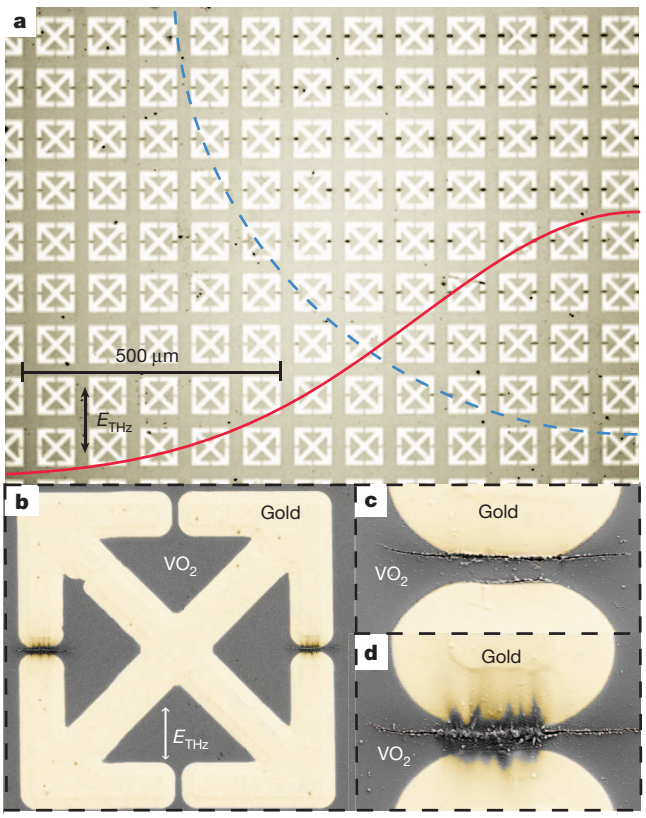

Figure 4 | THz-field-induced damage as revealed by optical and scanning electron micrographs. **a**, Millimetre-scale optical image of damage to VO_2 in the SRR gaps. The black dots are damaged VO_2. The dashed blue circle approximates the THz beam waist, and the red curve approximates the THz intensity profile. **b**, SEM image of a single SRR reveals that VO_2 is damaged by the vertically polarized THz field. **c** and **d**, Expanded view of damage at the edge of the THz beam (**c**) and near the beam centre (**d**). The gold SRRs were post-processed with false colour.

mechanism in our experiments. The large nonlinear transmission shown in Fig. 2 for the THz pump and in Fig. 3 for the THz probe is observed only within ~30 K of the transition temperature of 340 K, in the present experimental conditions. Note that a 1 MV cm^{-1} in-gap THz field corresponds to a THz fluence of ~2 mJ cm^{-2}, which is similar to the typical fluence threshold of the optically (800 nm) induced IMT[12,13,28]. The very different excitation wavelengths act initially on the system in very different ways, driving the short-time responses through different mechanisms. The extent of lattice heating that sustains the metallic phase at longer times may be comparable.

At our highest in-gap electric fields of ~4 MV cm^{-1} (~30 mJ cm^{-2} fluence), the THz electric field causes irreversible damage to the VO_2 metamaterials. Damage to the VO_2 thin film in the horizontal side gaps can be seen as black dots in Fig. 4a, with close-up images of the damage shown in Fig. 4b–d. The damage pattern depends strongly on the field strength, increasing towards the beam centre. The unique SRR geometry allows approximate visualization of the THz electric field, as the damage pattern follows the equipotential lines of the field (Supplementary Fig. 2).

In summary, we have demonstrated a THz-driven insulator–metal phase transition and shown that in VO_2 it is initiated by Poole–Frenkel electron liberation, followed by lattice equilibration on a picosecond timescale. Our work shows that metamaterial-enhanced high-field THz pulses can be used to study correlated-electron materials in a non-perturbative regime. The technique is extremely versatile, and can be used to study THz-induced phase transitions in other correlated materials and transition metal oxides (including high-T_c superconductors[29,30]), as well as THz-induced changes in electronic properties more generally. The metamaterial design can be optimized to balance the requirements in any particular measurement for maximum field enhancement, bandwidth and mode volume. Magnetic-field enhancement can also be studied, as SRRs provide temporal and spatial separation of the peak electric and magnetic fields.

METHODS SUMMARY

Metamaterial fabrication. Metamaterials on VO_2 films were made by stencil deposition techniques. The shadow masks used as stencils were made from 400-nm silicon nitride films with engraved metamaterial patterning. Once the masks were made, no photolithography was needed for the metamaterial fabrication onto the VO_2 surface. This prevented chemical contamination, thus ensuring high-quality samples.

High-field THz pulse generation and measurement. The output of a 1-kHz, 6.5-W, 100-fs Ti:sapphire amplifier was used to generate nearly single-cycle THz pulses by optical rectification in a lithium niobate crystal with the tilted pulse front technique. Our peak THz field strength was measured to be 300 kV cm^{-1}, with an estimated spot size of 1.5 mm. We used a standard electro-optic sampling setup to measure time-dependent fields. The THz field and a femtosecond optical pulse were overlapped spatially on a ZnTe electro-optic crystal, and the THz-induced optical birefringence was measured as the femtosecond pulse arrival time was varied, yielding the THz field temporal profile as in Fig. 2b (blue curve). Fourier transformation yielded the transmitted THz field in the frequency range 0.2–2.5 THz. Measurements with different THz pump–probe time delays yielded the two-dimensional data shown in Fig. 3a. All the experiments were performed in a high-vacuum cryostat with temperature control.

Electromagnetic simulations. The simulations in Fig. 2a–c, e and Supplementary Fig. 2d were performed using CST Microwave Studio 2011. All simulations used extremely fine mesh-cell settings, determined by adaptive meshing results (up to 8 million). All the parameters used in the CST simulations were those reported from experimental measurements; for example, the conductivity in the insulating state at 320 K is 10 $(\Omega\,\mathrm{cm})^{-1}$ and the relative permittivity of VO_2 in the insulating state is ~10. The simulations were performed using a time-domain transient solver.

Received 29 January; accepted 14 May 2012.
Published online 11 July 2012.

1. Morin, F. J. Oxides which show a metal-to-insulator transition at the Neel temperature. *Phys. Rev. Lett.* **3,** 34–36 (1959).
2. Limelette, P. *et al.* Universality and critical behavior at the Mott transition. *Science* **302,** 89–92 (2003).
3. Asamitsu, A., Tomioka, Y., Kuwahara, H. & Tokura, Y. Current switching of resistive states in magnetoresistive manganites. *Nature* **388,** 50–52 (1997).
4. Wang, J. *et al.* Epitaxial $BiFeO_3$ multiferroic thin film heterostructures. *Science* **299,** 1719–1722 (2003).
5. Cao, J. *et al.* Strain engineering and one-dimensional organization of metal-insulator domains in single-crystal vanadium dioxide beams. *Nature Nanotechnol.* **4,** 732–737 (2009).
6. Liu, M. K. *et al.* Photoinduced phase transitions by time resolved far-infrared spectroscopy in V_2O_3. *Phys. Rev. Lett.* **107,** 066403 (2011).
7. Cavalleri, A. *et al.* Femtosecond structural dynamics in VO_2 during an ultrafast solid-solid phase transition. *Phys. Rev. Lett.* **87,** 237401 (2001).
8. Berglund, C. N. & Guggenheim, H. J. Electronic properties of VO_2 near the semiconductor-metal transition. *Phys. Rev.* **185,** 1022–1033 (1969).
9. Stefanovich, G., Pergament, A. & Stefanovich, D. Electrical switching and Mott transition in VO_2. *J. Phys. Condens. Matter* **12,** 8837–8845 (2000).
10. Merbold, H., Bitzer, A. & Feurer, T. Second harmonic generation based on strong field enhancement in nanostructured THz materials. *Opt. Express* **19,** 7262–7273 (2011).
11. Chen, H.-T. *et al.* Active terahertz metamaterial devices. *Nature* **444,** 597–600 (2006).
12. Kübler, C. *et al.* Coherent structural dynamics and electronics correlations during an ultrafast insulator-to-metal phase transition in VO_2. *Phys. Rev. Lett.* **99,** 116401 (2007).
13. Hilton, D. J. *et al.* Enhanced photosusceptibility near T_c for the light-induced insulator-to-metal phase transition in vanadium dioxide. *Phys. Rev. Lett.* **99,** 226401 (2007).
14. Kim, H.-T. *et al.* Mechanism and observation of Mott transition in VO_2-based two- and three- terminal devices. *N. J. Phys.* **6,** 52 (2004).
15. Hoffmann, M. C., Hebling, J., Hwang, H. Y., Yeh, K.-L. & Nelson, K. A. THz-pump/THz-probe spectroscopy of semiconductors at high field strengths. *J. Opt. Soc. Am. B* **26,** A29–A34 (2009).
16. Yeh, K.-L., Hoffmann, M. C., Hebling, J. & Nelson, K. A. Generation of 10 μJ ultrashort THz pulses by optical rectification. *Appl. Phys. Lett.* **90,** 171121 (2007).
17. Hirori, H., Doi, A., Blanchard, F. & Tanaka, K. Single-cycle terahertz pulses with amplitudes exceeding 1 MV/cm generated by optical rectification in $LiNbO_3$. *Appl. Phys. Lett.* **98,** 091106 (2011).
18. Hoffmann, M. C., Hebling, J., Hwang, H. Y., Yeh K.-L. & Nelson K. A.. Impact ionization in InSb proved by terahertz pump-terahertz probe spectroscopy. *Phys. Rev. B* **79,** 161201 (2009).
19. West, K. G. *et al.* Growth and characterization of vanadium dioxide thin films prepared by reactive-based target ion beam deposition. *J. Vac. Sci. Technol. A* **26,** 133–139 (2008).
20. Werley, C. A. *et al.* Time-resolved imaging of near fields in THz antennas and direct quantitative measurement of field enhancements. *Opt. Express* **20,** 8551–8567 (2012).
21. Driscoll, T. *et al.* Memory metamaterials. *Science* **325,** 1518–1521 (2009).
22. Seo, M. A. *et al.* Terahertz field enhancement by a metallic nano slit operating beyond the skin-depth limit. *Nature Photon.* **3,** 152–156 (2009).
23. Shalaby, M. *et al.* Concurrent field enhancement and high transmission of THz radiation in nanoslit arrays. *Appl. Phys. Lett.* **99,** 041110 (2011).
24. Simmons, J. G. Poole-Frenkel effect and Schottky effect in metal-insulator-metal systems. *Phys. Rev.* **155,** 657–660 (1967).
25. Yeargan, J. R. & Taylor, H. L. The Poole-Frenkel effect with compensation present. *J. Appl. Phys.* **39,** 5600–5604 (1968).
26. Pergament, A., Boriskov, P. P., Velichko, A. A. & Kuldin, N. A. Switching effect and the metal-insulator transition in electric field. *J. Phys. Chem. Solids* **71,** 874–879 (2010).
27. Groeneveld, R. H. M., Sprik, R. & Lagendijk, A. Femtosecond spectroscopy of electron-electron and electron-phonon energy relaxation in Ag and Au. *Phys. Rev. B* **51,** 11433–11445 (1995).
28. Pashkin, A. *et al.* Ultrafast insulator-metal phase transition in VO_2 studied by multiterahertz spectroscopy. *Phys. Rev. B* **83,** 195120 (2011).
29. Basov, D. N. *et al.* Electrodynamics of correlated electron materials. *Rev. Mod. Phys.* **83,** 471–541 (2011).
30. Qazilbash, M. M. *et al.* Mott transition in VO_2 revealed by infrared spectroscopy and nano-imaging. *Science* **318,** 1750–1753 (2007).

Supplementary Information is linked to the online version of the paper at www.nature.com/nature.

Acknowledgements We acknowledge support from DOE-BES under grant DE-FG02-09ER46643 and from ONR grant N00014-09-1-1103.

Author Contributions R.D.A., K.A.N, M.L. and H.Y.H. came up with the experimental idea. H.Y.H. and M.L. performed the experiments. H.T., K.F., M.L., F.G.O. and X.Z. fabricated the metamaterial structures. A.J.S., M.L. and H.Y.H. performed full-wave electromagnetic simulation and analysed the data. K.G.W., S.K., J.L. and S.A.W. prepared the VO_2 thin films. A.C.S. and G.R.K. assisted with the simulation. M.L., H.Y.H., R.D.A. and K.A.N. wrote the manuscript. All authors contributed to the understanding of the underlying physics.

Author Information Reprints and permissions information is available at www.nature.com/reprints. The authors declare no competing financial interests. Readers are welcome to comment on the online version of this article at www.nature.com/nature. Correspondence and requests for materials should be addressed to. K.A.N. (kanelson@mit.edu) or R.D.A. (raveritt@buphy.bu.edu).